

Analysis of a distributed model of leg coordination

I. Individual coordination mechanisms

Alan Calvitti¹, Randall D. Beer^{1,2}

¹Department of Electrical Engineering and Computer Science, Case Western Reserve University, Cleveland, OH 44106, USA

²Department of Biology, Case Western Reserve University, Cleveland, OH 44106, USA

Received: 22 June 1999 / Accepted in revised form: 7 September 1999

Abstract. Using tools from discrete dynamical systems theory, we begin a systematic analysis of a distributed model of leg coordination with both biological and robotic applications. In this paper, we clarify the role of individual coordination mechanisms by studying a system of two leg oscillators coupled in one direction by each of the three major mechanisms that have been described for the stick insect *Carausius morosus*. For each mechanism, we derive analytical return maps, and analyze the behavior of these return maps under iteration in order to determine the asymptotic phase relationship between the two legs. We also derive asymptotic relative phase densities for each mechanism and compare these densities to those obtained from numerical simulations of the model. Our analysis demonstrates that, although each of these mechanisms can individually compress a range of initial conditions into a narrow band of relative phase, this asymptotic relative phase relationship is, in general, only neutrally stable. We also show that the nonlinear dependence of relative phase on walking speed along the body in the full hexapod model can be explained by our analysis. Finally, we provide detailed parameter charts of the range of behavior that each mechanism can produce as coupling strength and walking speed are varied.

1998), where the position at which a leg switches state is influenced by the state of adjacent legs via a specific network of coordination mechanisms. An important feature of this model is that it is highly distributed. Gaits arise not from a centralized gait generator, but rather from interactions between the individual leg oscillators mediated by the network of coordination mechanisms. Although this model was originally developed for the stick insect *Carausius morosus*, variations of it have also been successfully applied to walking in the crayfish *Astacus leptodactylus* (Müller and Cruse 1991) and to slow walking in the cat (Cruse and Warnecke 1992). This model has also been employed to generate insect-like gaits in a variety of legged robots (Espenschied et al. 1993; Ferrell 1995; Pfeiffer et al. 1995; Espenschied et al. 1996; Flannigan et al. 1998; Frik 1999).

The goal of this paper is to begin a systematic analysis of this model of leg coordination. Although extensive simulation studies of this model have been performed (Dean 1991a,b, 1992a,b), much is still unknown about the general dynamical behavior of this model and the dependence of this behavior on parameters. As a consequence, parameters associated with the model must be tuned heuristically to achieve a desired behavior (Espenschied et al. 1993; Cruse et al. 1995; Ferrell 1995; Cymbalyuk et al. 1998). In this paper, we study the behavior of each of the three major coordination mechanisms in isolation. Specifically, we derive analytical return maps for each of the mechanisms, study the asymptotic form of these return maps, and characterize their layout in parameter space. In addition, we demonstrate how to calculate the asymptotic relative phase density for each mechanism, which gives the probability of observing any particular phase relationship as walking speed and coupling strength are varied. The effects of combining multiple mechanisms, as well as two-way interactions between multiple leg oscillators, will be examined in future papers.

1 Introduction

Coordinating the movements of individual legs so as to maintain a stable gait is one of the central problems that must be solved by any walking animal or robot. Experimental studies of the consequences of perturbations during walking in the stick insect (Bässler 1983; Graham 1985) have led to a series of models of leg coordination in walking arthropods (Graham 1977; Cruse 1979, 1980). We will focus on the most recent version of the model here (Cruse 1990; Cruse et al.

2 Model

Each leg oscillator L is a hybrid dynamical system (Johnson 1994) characterized by a continuous position

Correspondence to: R.D. Beer (e-mail: beer@alpha.ces.cwru.edu, Tel.: +1-216-3682816, Fax: +1-216-3682801)

$x \in \mathbb{R}$ in leg-centered coordinates and a discrete velocity $\dot{x} \in \{v_p, v_r\} : L(t) = (x(t), \dot{x}(t))$. When a leg is in protraction, it is lifted from the ground and swinging forward relative to the body with a constant velocity $v_p > 0$. When a leg is in retraction, it is on the ground, providing support and swinging backward relative to the body with a constant velocity $v_r < 0$. As in many walking animals, v_p is relatively constant in the stick insect, while v_r varies according to walking speed (Graham 1972). A protracting leg switches to retraction when it crosses an anterior extreme position (AEP). Likewise, a retracting leg switches to protraction when it crosses a posterior extreme position (PEP). The i th leg oscillator is described by the equation

$$\dot{x}_i = \begin{cases} v_r & \text{if } (\dot{x}_i = v_p) \text{ and } (x_i \geq \text{AEP}_i) \\ v_p & \text{if } (\dot{x}_i = v_r) \text{ and } (x_i \leq \text{PEP}_i) \\ \dot{x}_i & \text{otherwise} \end{cases} . \quad (1)$$

Interleg coordination mechanisms operate by modifying the AEP or PEP of a receiving leg depending upon the state of a sending leg. Six different mechanisms have been described for the stick insect (Cruse et al. 1995). However, a subset of three of these mechanisms has been used by many authors and is known to be sufficient for generating a full range of insect-like gaits (Espenschied et al. 1993), so we concentrate on this subset here. Since these three mechanisms only modify the PEP of a receiving leg, we set AEP to a constant intrinsic value (IAEP) for all legs. In addition, all leg oscillators have an associated constant intrinsic PEP value (IPEP) against which the coordination mechanisms operate. In this paper, we set IAEP = 1 and IPEP = -1. Note that there is some variation in how these mechanisms are implemented in the literature, and some authors do not fully specify their implementation. We have chosen to analyze the simplest form consistent with the original model which produces the full range of gaits.

During protraction in a sending leg, mechanism 1 delays the start of protraction in a receiving leg by shifting the latter's PEP backward (Fig. 1A):

$$M_1(x_i, \dot{x}_i) = \begin{cases} 1 & \text{if } \dot{x}_i = v_p \\ 0 & \text{otherwise} \end{cases} , \quad (2)$$

where the associated coupling strength of this mechanism is $\alpha_1 \leq 0$ since it delays the phase of a receiving leg when active.

Immediately following the beginning of retraction in a sending leg, mechanism 2 briefly advances the start of protraction in a receiving leg by shifting the latter's PEP forward (Fig. 1A):

$$M_2(x_i, \dot{x}_i) = \begin{cases} 1 & \text{if } (\dot{x}_i = v_r) \text{ and } ((1 - c) \text{IAEP} \leq x_i \leq \text{IAEP}) \\ 0 & \text{otherwise} \end{cases} , \quad (3)$$

where M_2 is only active for a small range of leg positions determined by the constant $0 < c < 1$. In this paper, we set $c = 0.1$. Note that some authors characterize M_2 by means of a duration rather than the position of the sending leg

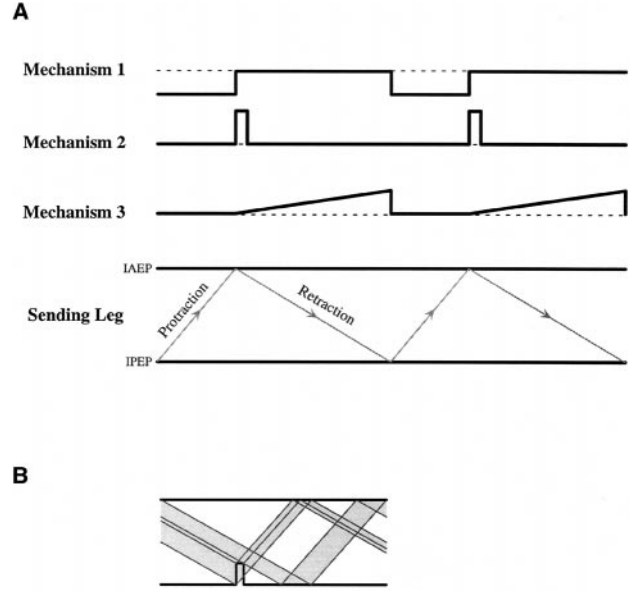


Fig. 1. **A** A schematic illustration of the three coordination mechanisms analyzed in this paper. As a sending leg alternates between protraction and retraction, each mechanism modifies the posterior extreme position (PEP) of a receiving leg as shown. **B** An illustration of “shadowing” in mechanism 2. Due to the positive-going nature of this mechanism, no trajectory can bounce off of the trailing edge of the mechanism or the first part of the immediately following segment. Note how this shadowing splits a continuous set of trajectories into two distinct subsets

(Espenschied et al. 1993), but our approach has the advantage of not requiring an external clock. The associated coupling strength of this mechanism is $\alpha_2 \geq 0$, since it advances the phase of the receiving leg when active.

Throughout the retraction of a sending leg, mechanism 3 advances the start of protraction in a receiving leg by shifting the latter's PEP increasingly forward (Fig. 1A):

$$M_3(x_i, \dot{x}_i) = \begin{cases} (\text{IAEP} - x_i) / |\text{IAEP} - \text{IPEP}| & \text{if } \dot{x}_i = v_r \\ 0 & \text{otherwise} \end{cases} , \quad (4)$$

The associated coupling strength of this mechanism is $\alpha_3 \geq 0$, since it advances the phase of the receiving leg when active. Some authors give α_3 a nonlinear velocity dependence (Cruse et al. 1998; Cymbalyuk et al. 1998), but we do not consider this complication here.

In the full hexapod model, the coordination mechanisms that impinge on the i th leg oscillator modulate its PEP as:

$$\text{PEP}_i = \text{IPEP} + \sum_{j=1}^6 \alpha_1^{ji} M_1(x_j, \dot{x}_j) + \alpha_2^{ji} M_2(x_j, \dot{x}_j) + \alpha_3^{ji} M_3(x_j, \dot{x}_j) \quad i = 1, \dots, 6 , \quad (5)$$

where α_k^{ji} is the coupling strength of mechanism k from the j th to the i th leg oscillators. Note that a PEP modulation is only “felt” by a receiving leg when that leg is in retraction. When the leg is in protraction, its trajectory will pass unaffected through the PEP (see Fig. 3A for examples of this for mechanism 1).

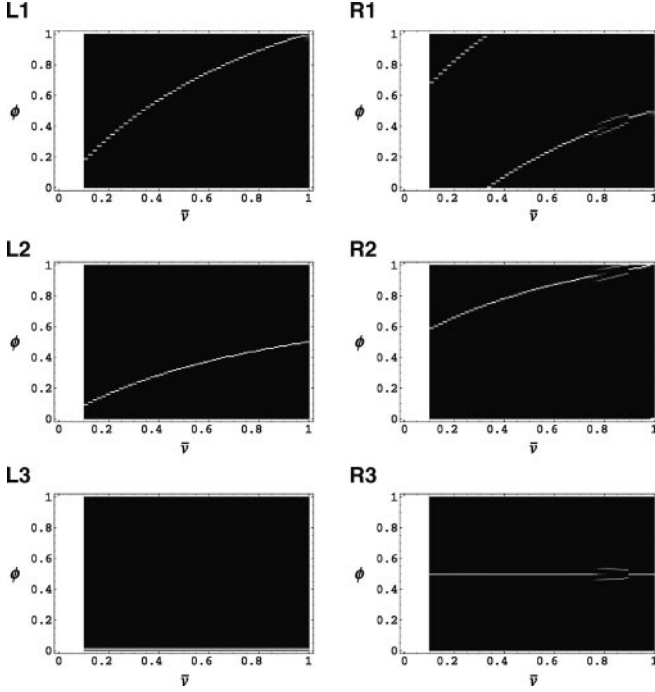


Fig. 2. Asymptotic relative phase density plots for a simulation of the full hexapod model as normalized walking speed \bar{v} is varied. The relative phase ϕ between two legs is defined in Sect. 2. Brighter regions correspond to more likely phase relationships. The plots are labeled L for left side of the body and R for right side, and the legs are numbered from 1 (front) to 3 (back). All phases are defined relative to L_3 . In these simulations, all coupling strengths were 0 except $\alpha_1^{L3,L2} = \alpha_1^{L2,L1} = \alpha_1^{R3,R2} = \alpha_1^{R2,R1} = -0.6$, $\alpha_2^{L3,L2} = \alpha_2^{L2,L1} = \alpha_2^{R3,R2} = \alpha_2^{R2,R1} = 1$, $\alpha_3^{L1,L2} = \alpha_3^{L2,L3} = \alpha_3^{R1,R2} = \alpha_3^{R2,R3} = 0.6$, $\alpha_2^{L1,R1} = \alpha_2^{R1,L1} = \alpha_2^{L2,R2} = \alpha_2^{R2,L2} = \alpha_2^{L3,R3} = \alpha_2^{R3,L3} = 0.1$, and $\alpha_3^{L1,R1} = \alpha_3^{R1,L1} = \alpha_3^{L2,R2} = \alpha_3^{R2,L2} = \alpha_3^{L3,R3} = \alpha_3^{R3,L3} = 0.9$. These values were slightly modified from Espenschied et al. (1993). In order to produce these plots, 50 different velocity values equally spaced in the range $[0.1, 1]$ were simulated (because it takes too long in simulation to reach the asymptotic relative phase for $\bar{v} < 0.1$ the plots are blank below this value). For each velocity slice, 100 initial conditions uniformly distributed in $[\text{IPEP}, \text{IAEP}] \times \{v_p, v_r\}$ were integrated using the explicit Euler method with a step size of 0.01 s. Each run was integrated for 100 s to allow transients to pass and then ϕ statistics were collected for the next 200 s. To estimate the densities, the mean ϕ for each run was computed using circular statistics and binned using a bin size of 0.0075

In the stick insect, M_1 and M_2 are directed forward along the body, M_3 is directed backward along the body, and M_2 and M_3 operate symmetrically across the body (Cruse 1990; Cruse et al. 1998). Although distinct coupling strengths could, in principle, be assigned to each connection, both experimental evidence and symmetry considerations suggest that the coupling strength of any given mechanism is only distinguished by whether a connection is ipsilateral or contralateral. When these coupling strengths are set appropriately, simulations of the full hexapod model exhibit a nonlinear dependence of relative phase on walking speed along the body (Fig. 2L2) and a constant average relative phase of $1/2$ across the body (Fig. 2R3). Note that, for $\bar{v} \equiv -v_r/v_p$ between about 0.75 and 0.8, three distinct crossbody

phase relationships seem to be stable, while for \bar{v} between about 0.8 and 0.9, two distinct crossbody phase relationships seem to be stable (Fig. 2R1–2R3). While the phase difference is small (and therefore unlikely to be obvious in the stepping pattern), this is the kind of dynamical behavior that we would ultimately like to understand.

In order to study the phase-locking behavior of the individual coordination mechanisms, in this paper we focus on two leg oscillators L_1 and L_2 coupled in one direction by one of the three mechanisms (Fig. 3A). L_1 is the sending leg oscillator, with $\text{PEP}_1 = \text{IPEP}$, and L_2 is the receiving leg oscillator, with $\text{PEP}_2 = \text{IPEP} + \alpha_k M_k(x_1, \dot{x}_1)$ for $k = 1, 2$, or 3. Both oscillators share the same IAEP, IPEP, v_r and v_p .

Our analysis focuses on the relative phase ϕ between L_1 and L_2 , and especially the asymptotic value ϕ^* that this relative phase adopts after transients have passed. If τ_i is the time of onset of protraction in the i th leg oscillator, $D \equiv |\text{IAEP} - \text{IPEP}|$ is the range of motion of an uncoupled leg, and $T_1 = D/|v_p| + D/|v_r|$ is the period of L_1 , then $\phi \equiv (\tau_2 - \tau_1)/T_1$. Note that ϕ is only defined when L_2 initiates protraction exactly once within the time interval $[\tau_1, \tau_1 + T_1]$. In general, both ϕ and ϕ^* will depend on the initial state $L_2(0) = (x_2(0), \dot{x}_2(0))$ of the receiving leg oscillator, on the coupling strength α_i , and on the normalized walking speed $\bar{v} = -v_r/v_p$ (since ϕ is invariant to time rescaling, only the ratio of retraction and protraction velocities matters). Note that the duty factor (defined as retraction duration over step period), a common descriptive parameter of insect gaits, can be expressed as $1/(\bar{v} + 1)$.

3 Mechanism 1

During protraction in L_1 , mechanism 1 delays the start of protraction in L_2 by shifting its PEP backward by an amount α_1 (Fig. 3A). Simulation results demonstrating how the density of ϕ^* varies with \bar{v} for two different values of α_1 are shown in Fig. 4B1 and 4C1. Note that, unlike in the full hexapod model (Fig. 2L2), the two leg oscillators do not adopt a single phase relationship. However, for some values of α_1 , M_1 does asymptotically compress the phase relationship into a narrow band exhibiting a nonlinear dependence on walking speed similar to that observed along the body in the full hexapod model (compare white band in Fig. 4B1 to Fig. 2L2). Our goal here is to develop a complete mathematical understanding of simulation results such as these and to clarify the underlying dynamics. Initially, we will focus on one particular set of parameter values $(\bar{v}, \alpha_1) = (0.9, -0.5)$ in order to illustrate our approach. Then we will show how these results vary parametrically.

The primary tool that we will use in our analysis is the return map Σ , which describes how the state of L_2 changes from one cycle of L_1 to the next (Fig. 3). Formally, the first return map $\Sigma : [\text{IPEP}, \text{IAEP}] \times \{v_p, v_r\} \rightarrow [\text{IPEP}, \text{IAEP}] \times \{v_p, v_r\}$ maps the state $L_2(\tau_1)$ at the onset of protraction at time τ_1 in L_1 to the state $L_2(\tau_1 + T_1)$ at the onset of the next protraction at time $\tau_1 + T_1$ in L_1 . Since

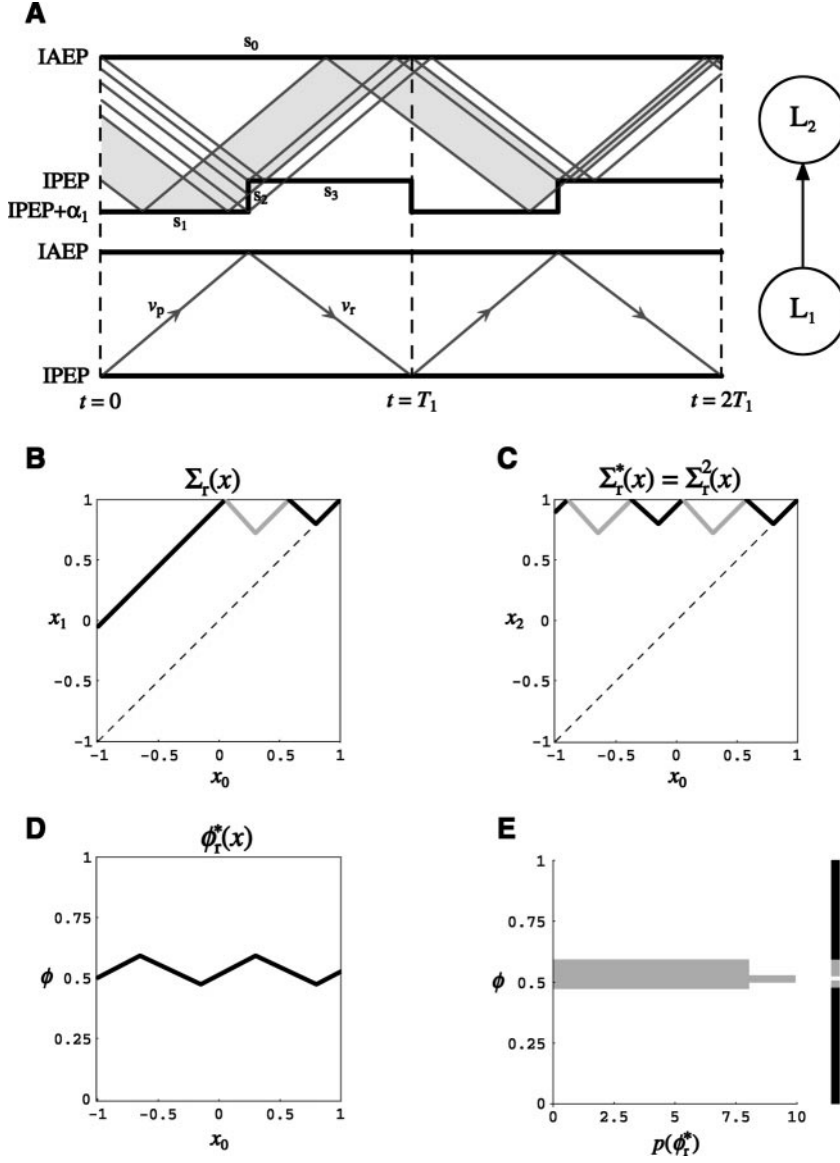


Fig. 3A–E. An analysis of mechanism 1 for $(\bar{v}, \alpha_1) = (0.9, -0.5)$. **A** Example trajectories of the receiving leg L_2 for two cycles of the sending leg L_1 . **B** The first retraction return map Σ_r . The segments are colored *gray* or *black* according to whether the leg returns in protraction or retraction, respectively. Note that the first protraction return map Σ_p is not shown because it is the trivial identity map. Also note that the trajectories shown in (A) correspond to the endpoints of the five segments of Σ_r shown here. **C** The asymptotic retraction return map Σ_r^* formed by composing Σ_r with itself. **D** The asymptotic relative phase map ϕ_r^* . **E** The asymptotic relative phase density $p(\phi_r^*)$ shown as both a histogram (*left*) and a density plot (*right*). Note that the histogram is placed sideways to emphasize its relationship to ϕ_r^* in (D)

the velocity is quantized, it is convenient to split Σ into two piecewise linear “colored” maps $\Sigma_p, \Sigma_r : [\text{IPEP}, \text{IAEP}] \rightarrow [\text{IPEP}, \text{IAEP}] \times \{v_p, v_r\}$, such that $\Sigma_p(x) = \Sigma(x, v_p)$ and $\Sigma_r(x) = \Sigma(x, v_r)$. The maps are colored in the sense that we shade them gray at all x for which the \dot{x}_2 component of $\Sigma_p(x)$ or $\Sigma_r(x)$ is v_p and we shade them black at all x for which the \dot{x}_2 component of $\Sigma_p(x)$ or $\Sigma_r(x)$ is v_r . This allows us to draw Σ_p and Σ_r as two one-dimensional maps. It turns out that the protraction return map is the trivial identity map $\Sigma_p(x) = (x, v_p)$, but Σ_r has a nontrivial structure (Fig. 3B).

We can calculate Σ_r from $L_1(t)$ and $L_2(t)$ as follows. With initial conditions $L_1(0) = (\text{IPEP}, v_p)$, $L_1(t)$ can be expressed as:

$$L_1(t) = (x_1(t), \dot{x}_1(t)) = \begin{cases} (\text{IPEP} + v_p(t \bmod T_1), v_p) & \text{if } (t \bmod T_1) \leq D/|v_p| \\ (\text{IPEP} + v_r((t - D/|v_p|) \bmod T_1), v_r) & \text{otherwise} \end{cases} \quad (6)$$

Once $L_1(t)$ is known, $\text{PEP}_2(t)$ can be expressed as:

$$\text{PEP}_2(t) = \begin{cases} \text{IPEP} + \alpha_1 & \text{if } (t \bmod T_1) \leq D/|v_p| \\ \text{IPEP} & \text{otherwise} \end{cases} \quad (7)$$

L_2 can now be treated as a periodically forced oscillator. Given $L_2(0) = (x_2(0), \dot{x}_2(0))$, $L_2(t)$ is determined by the solution of a series of piecewise linear algebraic equations that define the sequence of intersections between the trajectory and IAEP and $\text{PEP}_2(t)$. Over a single cycle, IAEP defines a single line segment s_0 and $\text{PEP}_2(t)$ is composed of three line segments s_1, s_2 and s_3 (Fig. 3A). For this particular setting of parameters, all initial positions $\text{IAEP} \leq x \leq \text{IPEP}$ that begin in retraction will exhibit one of the following five sequences of intersections: $\{s_3, s_0\}$, $\{s_2, s_0\}$, $\{s_2\}$, $\{s_1\}$, $\{s_1, s_0\}$. Therefore, the initial leg positions can be partitioned into five equivalence classes such that all trajectories within a given class undergo the same sequence of intersections. For example, the set of trajectories shown in light gray in Fig. 3A begin in retraction, intersect s_1 , bounce off of

s_0 , and then cross $t = T_1$ in retraction. The border points between such sets of trajectories are defined by the preimages of the endpoints of the segments s_0, s_1, s_2 and s_3 (dark gray lines in Fig. 3A). Each linear piece of Σ_r corresponds to one of the five possible equivalence classes (Fig. 3B):

$$\Sigma_r(x) = \begin{cases} (x - \alpha_1 \bar{v} - \alpha_1, v_r) & \text{if } -1 \leq x \leq \alpha_1 \bar{v} + \alpha_1 + 1 \\ ((-x + \alpha_1 + 1)/\bar{v} + \alpha_1 + 1, v_p) & \text{if } \alpha_1 \bar{v} + \alpha_1 + 1 \leq x \leq 2\bar{v} + \alpha_1 - 1 \\ (x - 2\bar{v} + 2/\bar{v}, v_p) & \text{if } 2\bar{v} + \alpha_1 - 1 \leq x \leq 2\bar{v} - 2/\bar{v} + 1 \\ (-\bar{v}x + 2\bar{v}^2 + \bar{v} - 1, v_r) & \text{if } 2\bar{v} - 2/\bar{v} + 1 \leq x \leq 2\bar{v} - 1 \\ (x, v_r) & \text{if } 2\bar{v} - 1 \leq x \leq 1 \end{cases} \quad (8)$$

Note that, for simplicity, we have substituted $\text{IAEP} = 1$ and $\text{IPEP} = -1$ here and in (9) and (10) below. Note also that the black portion (x, v_r) of Σ_r lies along the diagonal, implying that Σ_r has a degenerate continuum of neutrally stable fixed points. This is a common feature of the return maps for all three mechanisms because they all contain constant pieces equal to IPEP .

In contrast, all initial states x that begin in protraction exhibit the intersection sequence $\{s_0, s_3\}$ and end in the state (x, v_p) without ever being influenced by mechanism 1. This is why the protraction return map Σ_p for mechanism 1 is the identity map. Indeed, any initial x whose trajectory intersects only IAEP and IPEP will be mapped back to itself after one period because L_1 and L_2 share the same v_p and v_r .

Since we are interested in the relationship of L_2 and L_1 many cycles in the future, we must study the higher iterates $\Sigma^n = L_2(nT_1)$ of the first return map Σ , which are formed by composing Σ with itself n times. Note that iterating Σ involves interleaving Σ_p and Σ_r whenever the velocity switches (i.e. whenever the \dot{x}_2 component of $\Sigma_p(x)$ is v_r or the \dot{x}_2 component of $\Sigma_r(x)$ is v_p). Figure 3A shows how the trajectories discussed above continue over a second cycle. We will refer to an iterated return map with the property that $\Sigma^{l+1} = \Sigma^l$ for some finite l as an asymptotic return map Σ^* , since the state of L_2 is the same at all future periods beyond l . Σ^* can also be split into two ‘‘colored’’ asymptotic return maps $\Sigma_p^*(x) = \Sigma^*(x, v_p)$ and $\Sigma_r^*(x) = \Sigma^*(x, v_r)$. Of course, $\Sigma_p^*(x) = \Sigma_p(x)$, but $\Sigma_r^*(x) = \Sigma_r^2(x)$ is given by (Fig. 3C):

$$\Sigma_r^*(x) = \begin{cases} (x - 2\alpha_1 \bar{v} - 2\alpha_1, v_r) & \text{if } -1 \leq x \leq 2\alpha_1 \bar{v} + 2\alpha_1 + 1 \\ ((-x + 2\alpha_1 + 1)/\bar{v} + 2\alpha_1 + 1, v_p) & \text{if } 2\alpha_1 \bar{v} + 2\alpha_1 + 1 \leq x \leq \alpha_1 \bar{v} + 2\bar{v} + 2\alpha_1 - 1 \\ (x + 2/\bar{v} - (\alpha_1 + 2)\bar{v} - \alpha_1, v_p) & \text{if } \alpha_1 \bar{v} + 2\bar{v} + 2\alpha_1 - 1 \leq x \leq -2/\bar{v} + (\alpha_1 + 2)\bar{v} + \alpha_1 + 1 \\ (-\bar{v}x + (\alpha_1 + 1)\bar{v} + (\alpha_1 + 2)\bar{v}^2 + 1, v_r) & \text{if } -2/\bar{v} + (\alpha_1 + 2)\bar{v} + \alpha_1 + 1 \leq x \leq (\alpha_1 + 2)\bar{v} + \alpha_1 - 1 \\ (x - \alpha_1 \bar{v} - \alpha_1, v_r) & \text{if } (\alpha_1 + 2)\bar{v} + \alpha_1 - 1 \leq x \leq \alpha_1 \bar{v} + \alpha_1 + 1 \\ \Sigma_r(x) & \text{if } \alpha_1 \bar{v} + \alpha_1 + 1 \leq x \leq 1 \end{cases} \quad (9)$$

Note that, for $x \geq \alpha_1 \bar{v} + \alpha_1 + 1$, Σ_r^* and Σ_r are identical, giving a total of nine pieces for Σ_r^* .

Given the definition of relative phase, ϕ^* can be computed directly from Σ^* . $\phi_p^*(x) = (x + 1)/(2\bar{v} + 2)$ and $\phi_r^*(x)$ is given by (Fig. 3D):

$$\phi_r^*(x) = \begin{cases} (x - 2\alpha_1 \bar{v} - 2\alpha_1 + 1)/(2\bar{v} + 2) & \text{if } -1 \leq x \leq (\alpha_1 + 2)\bar{v} + 2\alpha_1 - 1 \\ (-\bar{v}x + (\alpha_1 + 2)\bar{v}^2 + (\alpha_1 + 1)\bar{v})/(2\bar{v} + 2) & \text{if } (\alpha_1 + 2)\bar{v} + 2\alpha_1 - 1 \leq x \leq (\alpha_1 + 2)\bar{v} + \alpha_1 - 1 \\ (x - \alpha_1 \bar{v} - \alpha_1 + 1)/(2\bar{v} + 2) & \text{if } (\alpha_1 + 2)\bar{v} + \alpha_1 - 1 \leq x \leq 2\bar{v} + \alpha_1 - 1 \\ (-\bar{v}x + 2\bar{v}^2 + \bar{v})/(2\bar{v} + 2) & \text{if } 2\bar{v} + \alpha_1 - 1 \leq x \leq 2\bar{v} - 1 \\ (x + 1)/(2\bar{v} + 2) & \text{if } 2\bar{v} - 1 \leq x \leq 1 \end{cases} \quad (10)$$

Note that ϕ_r^* has fewer pieces than Σ_r^* because, although the velocity can switch as the trajectory moves from one sequence of intersections to another, the phase changes continuously. The folded nature of $\phi_r^*(x)$ is also interesting, illustrating how mechanism 1 acts to focus a large range of initial leg positions into a fairly small range of asymptotic relative phases. This effect can also clearly be seen Fig. 3A, where the set of trajectories in light gray are compressed into a much narrower range of leg positions after two cycles.

In order to summarize our analytical results for mechanism 1 and compare them to the simulation results (Fig. 4B1 and 4C1), we need to derive the density $p(\phi_r^*)$ of ϕ_r^* assuming a uniform density of initial leg positions x . This is accomplished by calculating how ϕ_r^* transforms a uniform density with range $[\text{IPEP}, \text{IAEP}]$. If Δx_i is the width of each piecewise linear segment of ϕ_r^* and $\Delta \phi_i$ is the corresponding height, then this density can be expressed as (Fig. 3E):

$$p(\phi_r^*) = \frac{1}{D} \sum_{i=1}^5 \left| \frac{\Delta x_i}{\Delta \phi_i} \right| = \begin{cases} 0 & \text{if } 0 \leq \phi \leq \bar{v}/(\bar{v} + 1) \\ 2/\bar{v} + 2\bar{v} + 4 & \text{if } \bar{v}/(\bar{v} + 1) \leq \phi \leq -\alpha_1 \\ 2/\bar{v} + 3\bar{v} + 5 & \text{if } -\alpha_1 \leq \phi \leq 1/(\bar{v} + 1) \\ 2/\bar{v} + 2\bar{v} + 4 & \text{if } 1/(\bar{v} + 1) \leq \phi \leq \bar{v}(2 - \alpha_1)/(2\bar{v} + 2) \\ 0 & \text{if } \bar{v}(2 - \alpha_1)/(2\bar{v} + 2) \leq \phi \leq 1 \end{cases} \quad (11)$$

This concludes our analysis of mechanism 1 for the particular parameter settings $(\bar{v}, \alpha_1) = (0.9, -0.5)$. We now describe how the results we have presented above vary with parameters. In order to understand the effects of coupling strength and walking speed on the behavior of mechanism 1, it is important to characterize the different forms that the first return maps Σ_p and Σ_r can take, as well as the layout of these different forms in parameter space. It turns out that Σ_p is always the identity map for mechanism 1 but, as \bar{v} and α_1 are varied, the individual linear pieces of Σ_r can merge or split as different ranges of initial positions undergo different sequences of intersections. The corresponding parameter chart contains five distinct regions, each corresponding to a qualitatively different form for Σ_r (black curves in Fig. 4A). Analytical expressions for Σ_r within each region can be derived as described above. For example, the expression for region II was given in (8). The boundaries between these regions can be calculated by solving for the locus of points in parameter space where the left and right border trajectories of an equivalence class coincide, giving the curves $\alpha_1 = -D\bar{v}$, $\alpha_1 = D(1 - 1/\bar{v})$ and $\alpha_1 = -D/(\bar{v} + 1)$. These boundaries all meet at the point $(\bar{v}, \alpha_1) = ((\sqrt{5} - 1)/2, 1 - \sqrt{5})$, where

multiple sets of equivalence class borders simultaneously coincide. Interestingly, the coordinates of this point are independent of the particular choice of IAEP and IPEP, suggesting that it is a deeper invariant of the model itself.

As the first return maps are iterated, additional boundaries can be introduced into the parameter chart (gray curves in Fig. 4A). These new boundaries separate regions of parameter space with qualitatively different asymptotic return maps. Interestingly, there is an infinite sequence of such boundaries for M_1 . Counting from the bottom, the n th thick gray boundary separates a region for which $\Sigma_r^* = \Sigma_r^n$ from one for which $\Sigma_r^* = \Sigma_r^{n+1}$. These boundaries take the form $\alpha_1 = -D\bar{v}/(n(\bar{v} + 1))$. Within region I, the thin gray boundaries $\alpha_1 = -D\bar{v}/((n-1)\bar{v} + n)$ further separate regions where Σ_r^* has $2n$ or $2n + 1$ pieces. Likewise, within region II, the thin gray boundaries $\alpha_1 = -D(1 - \bar{v} - \bar{v}^2)/((n-1)(\bar{v}^2 + \bar{v}))$, $\alpha_1 = -D\bar{v}/((n-1)\bar{v} + n)$ and $\alpha_1 = -D/(n(\bar{v} + 1))$ separate regions where Σ_r^* has $4n - 2$, $4n - 1$, $4n$ or $4n + 1$ pieces, respectively. Sample Σ_r^* for each region are shown on the right side of Fig. 4A.

The simulation results presented in Fig. 4B1 and 4C1 show how the asymptotic relative phase density for a

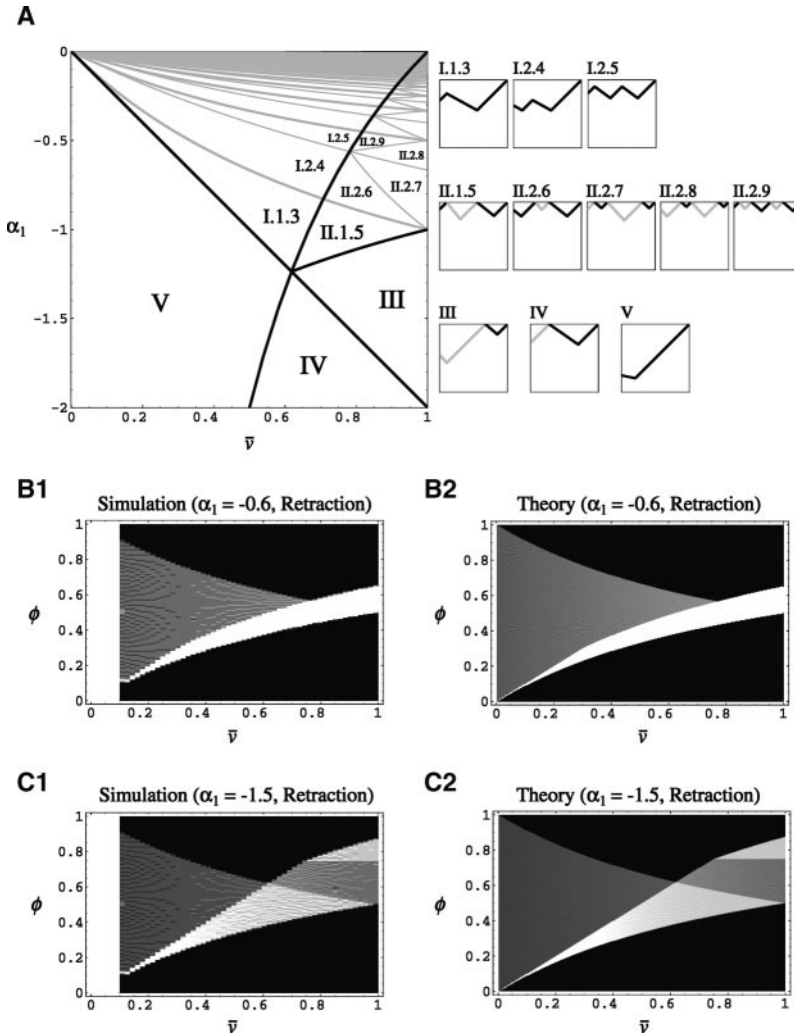


Fig. 4. A summary of analytical results for mechanism 1. **A** Chart of (\bar{v}, α_1) parameter space showing regions where Σ_r (black boundaries only) and Σ_r^* (both black and gray boundaries) take on qualitatively different forms. Thick gray boundaries separate regions where Σ_r requires different numbers of iterations to reach Σ_r^* , while thin gray boundaries further separate regions in which Σ_r^* contains differing numbers of pieces. Sample asymptotic return maps Σ_r^* for each region are shown to the right of the parameter chart (since Σ_p is always the trivial identity map, it is not shown). Note that there are infinite sequences of boundaries in regions I and II. These regions are labeled by two additional numbers which give the maximum number of iterations required to reach Σ_r^* and the number of distinct segments in Σ_r^* . **B** Simulated (B1) and theoretical (B2) plots of the dependence of $p(\phi_r^*)$ on \bar{v} for $\alpha_1 = -0.6$. **C** Simulated (C1) and theoretical (C2) plots of the dependence of $p(\phi_r^*)$ on \bar{v} for $\alpha_1 = -1.5$. In order to produce the simulation density plots shown in B1 and C1, 50 different velocity values equally spaced in the range $[0.1, 1]$ were simulated (because it takes too long in simulation to reach the asymptotic relative phase for $\bar{v} < 0.1$ the plots are blank below this value). For each velocity slice, 200 initial leg positions equally spaced between the intrinsic posterior extreme position (IPEP) and the intrinsic anterior extreme position (IAEP) were integrated using the explicit Euler method with a step size of 0.01 s. Each run was integrated for 50 s to allow transients to pass and then ϕ statistics were collected for the next 100 s. To estimate the densities, the mean ϕ for each run was computed using circular statistics and binned using a bin size of 0.0075

given α_1 varies with walking speed. In order to explain such results, we must likewise calculate the variation of $p(\phi_r^*)$ with \bar{v} analytically. As \bar{v} is varied, it may cross through several regions of the parameter chart. Analytical expressions for $p(\phi_r^*)$ within each region can be calculated as described above. Figure 4B2 and 4C2 show the theoretical $p(\phi_r^*)$ variation with \bar{v} corresponding to the simulation results presented in Fig. 4B1 and 4C1. As already mentioned, the white band in Fig. 4B2 has a dependence on \bar{v} similar to that observed along the body in the full hexapod model (Fig. 2L2). By decreasing α_1 , we can make this band as narrow as we like. However, as α_1 approaches 0, the number of steps required to reach this asymptotic relative phase becomes unbounded as $\lceil -D\bar{v}/(\alpha_1(\bar{v} + 1)) \rceil$.

4 Mechanism 2

Immediately following the start of retraction in L_1 , mechanism 2 briefly advances the start of protraction in L_2 by shifting its PEP forward by an amount α_2 (Fig. 1A). In this case, $\text{PEP}_2(t)$ can be expressed as:

$$\text{PEP}_2(t) = \begin{cases} \text{IPEP} + \alpha_2 & \text{if } D/|v_p| \leq t \bmod T_1 \leq \\ & D/|v_p| + \text{IAEP}(1-c)/|v_r| \\ \text{IPEP} & \text{otherwise} \end{cases} \quad (12)$$

Our analysis of mechanism 2 follows the same basic steps as detailed for mechanism 1. First, we derive analytical first return maps Σ_p and Σ_r from the intersections of $L_2(t)$ with IAEP and $\text{PEP}_2(t)$. Second, we derive the boundaries between qualitatively different first return maps in parameter space. Third, we derive asymptotic return maps Σ_p^* and Σ_r^* by iterating the first return maps until convergence. Fourth, we refine the parameter chart by deriving any new boundaries introduced by iteration. Fifth, we calculate the asymptotic relative phase ϕ^* corresponding to each asymptotic return map. Sixth, we calculate the corresponding asymptotic relative phase density $p(\phi^*)$. Finally, we calculate the variation of $p(\phi^*)$ with walking speed for comparison with simulations.

The major results for mechanism 2 are summarized in Fig. 5. Mechanism 2 raises a number of interesting new issues for analysis, all of which can be traced to the posi-

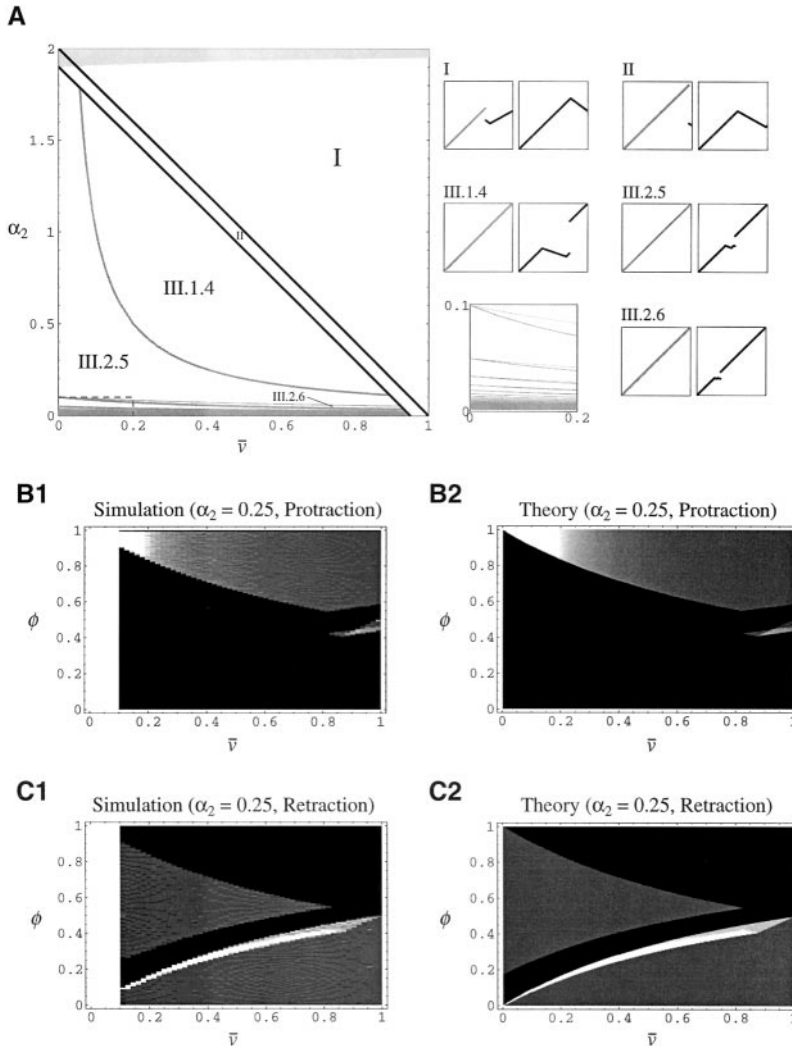


Fig. 5A–C. A summary of analytical results for mechanism 2. **A** Chart of (\bar{v}, α_2) parameter space showing regions where Σ (black boundaries only) and Σ^* (both black and gray boundaries) take on qualitatively different forms. Thick gray boundaries separate regions where Σ requires different numbers of iterations to reach Σ^* , while thin gray boundaries further separate regions in which Σ^* contains differing numbers of pieces. Sample (Σ_p^*, Σ_r^*) pairs of asymptotic return maps for each region are shown to the right of the parameter chart. Note that there are infinite sequences of boundaries in region III (see expanded view of dashed region at right). These regions are labeled by two additional numbers which give the maximum number of iterations required to reach Σ^* and the number of distinct segments in Σ^* . The light gray region at the top of the parameter chart shows where transient multiple stepping occurs, which we have not analyzed in detail. **B** Simulated (B1) and theoretical (B2) plots of the dependence of $p(\phi_p^*)$ on \bar{v} for $\alpha_2 = 0.25$. **C** Simulated (C1) and theoretical (C2) plots of the dependence of $p(\phi_r^*)$ on \bar{v} for $\alpha_2 = 0.25$. Simulation details were the same as in Fig. 4.

tive-going nature of this mechanism. Both Σ_p and Σ_r are nontrivial in general. $\text{PEP}_2(t)$ now consists of five line segments. However, no trajectory can bounce off the trailing edge of the active part of the mechanism or the first part of the following segment because they are “shadowed” by the mechanism (Fig. 1B). This shadowing introduces a discontinuity into the return maps because an arbitrarily small change to a trajectory can switch it from hitting the top of the mechanism to hitting IPEP.

The parameter chart for M_2 contains three regions where the first return maps Σ_p and Σ_r take on qualitatively different forms (Fig. 5A). These regions are separated by the boundaries $\alpha_2 = D(1 - \bar{v})$ and $\alpha_2 = D(1 - \bar{v}) - \text{IAEPC}$. As the return maps are iterated, an infinite sequence of new boundaries is introduced, as observed in M_1 . Counting from the top, the n th thick gray boundary separates a region for which $\Sigma_r^* = \Sigma_r^n$ from one for which $\Sigma_r^* = \Sigma_r^{n+1}$. These boundaries take the form $\alpha_2 = \text{IAEPC}/((n+1)\bar{v} + n)$. The thin gray boundaries $\alpha_2 = \text{IAEPC}/(n(\bar{v} + 1))$ further separate each of these regions into subregions where Σ_r^* has $2n + 1$ or $2n + 2$ pieces.

Another important difference for mechanism 2 is that transient multiple stepping can occur for some values of α_2 (light gray region in Fig. 5A). For example, when α_2 is sufficiently large, a trajectory can bounce between the top of mechanism 2 and IAEP multiple times before escaping. The boundary in parameter space above which transient multiple stepping can occur is given by the expression $\alpha_2 = D + \text{IAEPC}/(\bar{v} + 1)$. Since the strength of M_2 is approaching the leg excursion D above this boundary, we will not consider this region further here. However, it is interesting to note that multiple stepping has been observed in simulations of pairs of oscillators (Dean 1991a) and in experiments with stick insects (Cruse and Saxler 1980; Foth and Graham 1983).

Figure 5B2 and 5C2 show the theoretical $p(\phi^*)$ variation with \bar{v} corresponding to the simulation results presented in Fig. 5B1 and 5C1 for $\alpha_2 = 0.25$. Note that, under some conditions, M_2 asymptotically compresses the phase relationship into a narrow band exhibiting a nonlinear dependence on walking speed similar to that observed along the body in the full hexapod model (compare white band in Fig. 5C2 to Fig. 2L2). As α_2 approaches 0, ϕ_r^* is constrained to a narrower and narrower band, but the number of steps required to reach this asymptotic relative phase becomes unbounded as $\lceil (\text{IAEPC} - \alpha_2\bar{v})/(\alpha_2(\bar{v} + 1)) \rceil$.

5 Mechanism 3

Throughout the retraction of a sending leg, mechanism 3 advances the start of protraction in a receiving leg by shifting the latter’s PEP increasingly forward by an amount scaled by α_3 (Fig. 1A). In this case, $\text{PEP}_2(t)$ can be expressed as:

$$\text{PEP}_2(t) = \begin{cases} \text{IPEP} + \alpha_3(\text{IAEP} - x)/D & \text{if } t \bmod T_1 \geq D/|v_r| \\ \text{IPEP} & \text{otherwise} \end{cases} \quad (13)$$

Our analysis of mechanism 3 follows the same basic steps as did our analysis of M_1 and M_2 . The major results for mechanism 3 are summarized in Fig. 6. Like M_2 , mechanism 3 raises a number of interesting new issues for analysis, all of which can be traced to the graded and positive-going nature of this mechanism. Both Σ_p and Σ_r are again nontrivial in general and $\text{PEP}_2(t)$ now consists of three line segments. Shadowing due to the trailing edge of the mechanism once again produces discontinuities in the return maps. In addition, transient multiple stepping can occur for some initial conditions. A new feature introduced by mechanism 3 is that a unique asymptotic return map does not always exist and, when it does, in general it exists only in the limit, i.e. $\Sigma^* = \lim_{n \rightarrow \infty} \Sigma^n$.

The parameter chart for M_3 contains three regions where the first return maps Σ_p and Σ_r take on qualitatively different forms (Fig. 6A). These regions are separated by the boundaries $\alpha_3 = 2\bar{v}$ and $\alpha_3 = 4\bar{v}/(\bar{v}^2 + 1)$. In regions II and III, complex behavior can occur, including limit cycles and dynamics that are apparently chaotic (see the right side of Fig. 6A for an example of each). Since there is no well-defined phase relationship between the two leg oscillators in such cases, we have made no detailed study of these regions of parameter space.

Figure 6B2 and 6C2 show the theoretical $p(\phi^*)$ variation with \bar{v} corresponding to the simulation results presented in Fig. 6B1 and 6C1 for $\alpha_2 = 0.5$. Note that the simulation densities corresponding to the complex regions II and III exhibit no clear structure due to the complex dynamics possible within these regions. Clearly M_3 cannot be depended on for enforcing stable phase relationships at low walking speeds. Interestingly, although M_3 appears to exhibit a single stable fixed point for protraction (Fig. 6B2), this is not the case. As can be seen in the sample Σ_p^* for region I (right side of Fig. 6A), all initial conditions that begin in protraction are mapped to the upper edge of the neutrally stable region of Σ_r^* (thin white curve in Fig. 6C2). This edge is only half-stable. Any perturbation above this edge will indeed decay back down to it, but any perturbation below this edge will not return because it enters the neutrally stable region. Note that, once again, this thin white curve exhibits a nonlinear dependence on walking speed similar to that observed along the body in the full hexapod model (compare white curve in Fig. 6B2 and 6C2 to Fig. 2L2).

6 Discussion

In this paper, we have presented a systematic mathematical analysis of each of the three major coordination mechanisms employed in a distributed model of leg coordination with both biological and robotic applications. We showed how to derive piecewise linear first return maps for a system of two leg oscillators coupled in one direction by a single mechanism. By studying the behavior of these return maps under iteration, we determined the asymptotic phase relationship between the two legs, as well as how their asymptotic relationship varies with coupling strength and walking speed. Finally, because the final phase relationship is dependent

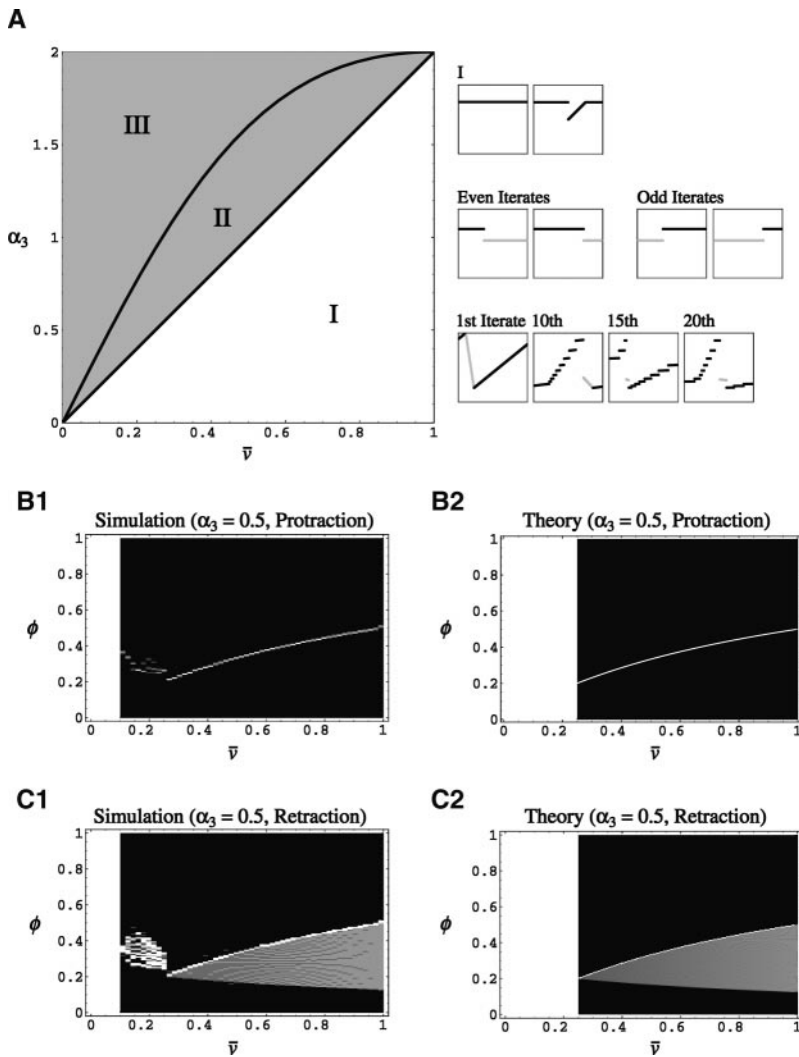


Fig. 6A–C. A summary of analytical results for mechanism 3. **A** Chart of (\bar{v}, α_3) parameter space showing regions where Σ take on qualitatively different forms (*black boundaries*). A sample (Σ_p^*, Σ_r^*) pair of asymptotic return maps for region I is shown at right. Regions II and III are colored *dark gray* because they contain complex dynamics whose detailed layout we have not analyzed. A sample (Σ_p^*, Σ_r^*) pair of asymptotic return maps from this region exhibiting a two-cycle is shown to the right, as are samples of higher iterates of a map from this region that appears to exhibit chaotic dynamics (note that only the retraction iterates $\Sigma_r, \Sigma_r^{10}, \Sigma_r^{15}$ and Σ_r^{20} are shown). **B** Simulated (B1) and theoretical (B2) plots of the dependence of $p(\phi_p^*)$ on \bar{v} for $\alpha_3 = 0.5$. **C** Simulated (C1) and theoretical (C2) plots of the dependence of $p(\phi_p^*)$ on \bar{v} for $\alpha_3 = 0.5$. Simulation details were the same as in Fig. 4 except that 100 s transients were discarded and ϕ statistics were collected for the next 200 s. Plots B2 and C2 are blank for $\bar{v} < 0.25$ because this is the point at which they intersect regions II and III, for which we do not have a detailed theoretical understanding

on initial conditions, we calculated how asymptotic relative phase density varies with normalized walking speed, assuming a uniform density on the initial leg states, and compared this to the results of numerical simulations of the model. A number of interesting features of these coupling mechanisms have been revealed by our analysis.

For the particular mechanisms that we have studied here, our parameter charts provide a detailed map of the range of behavior that each mechanism can produce. Because we have given exact expressions for all of the boundaries in these maps in terms of IAEP and IPEP (and c for M_2), it should be straightforward to apply these maps to small variations of the model. We have also given expressions for the maximum number of steps necessary to reach an asymptotic phase relationship, at least for M_1 and M_2 . Our analysis has also revealed a wealth of complexity. As coupling strength and walking speed are varied, there are infinite sequences of boundaries, regions of transient multiple stepping, phase oscillations and apparent chaos. While this complexity may appear surprising for such a simple model, it is worth noting that even the tent map, which consists of only two linear pieces, can exhibit the full complexity of

a period-doubling route to chaos (Devaney 1989). The potential for complex dynamics is only increased by the hybrid nature of the oscillator model (1).

Due to the piecewise constancy of portions of the coupling mechanisms, the return maps typically exhibit degenerate continua of fixed points, in which the asymptotic relative phase is only neutrally stable. Thus, it may be more appropriate to speak of phase compression in this model rather than phase locking. The apparent phase locking observed in the full hexapod network must arise from the cooperation of multiple mechanisms, as well as feedback between the leg oscillators. It is interesting to speculate how this might come about. For example, in the full network, M_1 and M_2 operate together in a rostral direction along the body. By comparing Fig. 4B2 and 5C2, we can see how these two mechanisms might have a complementary effect. In retraction, initial conditions that would normally end up below the white band in the absence of M_1 are mapped by M_1 into the white band (Fig. 4B2), while points that would normally end up in the narrow channel above the white band are mapped by M_2 to the white band (Fig. 5C2). Working together, it seems that these two mechanisms could act to at least partially stabilize the

white curve seen in Fig. 5C2, although these two mechanisms alone would still exhibit neutral stability within the gray funnel. However, a definitive understanding of the interaction between mechanisms must await an analysis of the complete network.

At least one feature of the full hexapod model can be explained by our analysis of the individual coordination mechanisms. We have repeatedly seen how the individual mechanisms compress a range of initial conditions into a narrow band of relative phase whose dependence on walking speed is strongly reminiscent of that observed in the full hexapod model (e.g., compare Figs. 4B2, 5C2, 6B2 and 6C2 to Fig. 2L2). Why does this occur? All three mechanisms have a rising edge at the point that L_1 switches from protraction to retraction (Fig. 1A). Under a wide range of conditions, all three mechanisms act to funnel initial conditions so that the onset of protraction in L_2 occurs at this point, whose relative phase is simply $(D/|v_p|)/T_1 = \bar{v}(\bar{v} + 1)$. This expression closely matches the shape of the asymptotic relative phase curve for L_2 in the full hexapod model (Fig. 2L2). Assuming that the same process occurs between L_2 and L_1 , the asymptotic relative phase of L_1 against L_3 would be $(D/|v_p| + D/|v_p|)/T_1 = 2\bar{v}/(\bar{v} + 1)$, which closely matches the curve for L_1 (Fig. 2L1).

Perhaps the most important contribution of the analysis described in this paper is the general framework that we have outlined for studying individual coordination mechanisms in Cruse's model. Our approach could be straightforwardly applied to variations of the mechanisms that we have considered here. For example, the importance of small implementation differences could be examined, such as using duration rather than position to determine the extent of the active portion of M_2 . The effect of a velocity-dependent gain in M_3 could also be studied. Our approach could also be applied to mechanisms that we have not considered here, such as mechanism 4 in the stick insect, by which one leg modifies the AEP of a more posterior leg (Cruse et al. 1998). In addition, our approach could be applied to combinations of mechanisms. Of particular interest are the combinations $M_1 + M_2$ (which operate in the rostral direction in the full hexapod network) and $M_2 + M_3$ (which operate across the body). It would also be interesting to explore the implications of our results for designing coordination mechanisms that stabilize a desired phase relationship. Of course, our ultimate goal is to understand the dynamics of the full hexapod network. This will require an extension of the approach we have described here because the feedback between legs makes it more difficult to use any one leg oscillator as a reference oscillator.

Acknowledgements. This work was supported in part by grants N00014-96-1-0708 and N0014-99-1-0378 from the Office of Naval Research. We thank Dr. Hillel Chiel for his comments on an earlier draft of this paper.

References

- Bässler U (1983) Neural basis of elementary behavior in stick insects. Springer Berlin Heidelberg New York
- Cruse H (1979) A new model describing the coordination pattern of the legs of a walking stick insect. *Biol Cybern* 32:107–113
- Cruse H (1980) A quantitative model of walking incorporating central and peripheral influences. II. The connections between the different legs. *Biol Cybern* 37:137–144
- Cruse H (1990) What mechanisms coordinate leg movement in walking arthropods? *Trends Neurosci* 13:15–21
- Cruse H, Saxler G (1980) The coordination of force oscillations and of leg movement in a walking insect. *Biol Cybern* 36:165–171
- Cruse H, Warnecke H (1992) Coordination of the legs of a slow-walking cat. *Exp Brain Res* 89:147–156
- Cruse H, Brunn DE, Bartling C, Dean J, Dreifert M, Kindermann T, Schmitz J (1995) Walking: a complex behavior controlled by simple networks. *Adapt Behav* 3:385–418
- Cruse H, Kindermann T, Schumm M, Dean J, Schmitz J (1998) Walknet—a biologically inspired network to control six-legged walking. *Neural Netw* 11:1435–1447
- Cymbalyuk GS, Borisyuk RM, Müller-Wilm U, Cruse H (1998) Oscillatory network controlling six-legged locomotion. Optimization of model parameters. *Neural Netw* 11:1449–1460
- Dean J (1991a) A model of leg coordination in the stick insect, *Carausius morosus*. I. Geometrical considerations of contralateral and ipsilateral coordination mechanisms between two adjacent legs. *Biol Cybern* 64:393–402
- Dean J (1991b) A model of leg coordination in the stick insect, *Carausius morosus*. II. Description of the kinematic model and simulation of normal step patterns. *Biol Cybern* 64:403–411
- Dean J (1992a) A model of leg coordination in the stick insect, *Carausius morosus*. III. Responses to perturbations of normal coordination. *Biol Cybern* 66:335–343
- Dean J (1992b) A model of leg coordination in the stick insect, *Carausius morosus*. IV. Comparisons of different forms of coordinating mechanisms. *Biol Cybern* 66:345–355
- Devaney RL (1989) An introduction to chaotic dynamical systems, 2nd edn. Addison-Wesley, Reading, Mass.
- Espenschied KS, Quinn RD, Chiel HJ, Beer RD (1993) Leg coordination mechanisms in stick insect applied to hexapod robot locomotion. *Adapt Behav* 1:455–468
- Espenschied KS, Quinn RD, Beer RD, Chiel HJ (1996) Biologically-based distributed control and local reflexes improve rough terrain locomotion in a hexapod robot. *Robot Auton Syst* 18:59–64
- Ferrell C (1995) A comparison of three insect-inspired locomotion controllers. *Robot Auton Syst* 16:135–159
- Flannigan WC, Nelson GM, Quinn RD (1998) Locomotion controller for a crab-like robot. *Proc 1998 IEEE International Conference on Robotics and Automation (ICRA'98)*, Belgium, May 18–21 IEEE pp 152–162
- Foth E, Graham D (1983) Influence of loading parallel to the body axis on the walking coordination of an insect. II. Contralateral effects. *Biol Cybern* 48:149–157
- Frik M, Quddat M, Karatas M, Losch CD (1999) A novel approach to autonomous control of walking machines. In: Virk GS, Randall M, Howard D (eds) *Proceedings of the 2nd International Conference on Climbing and Walking Robots CLAWAR 99*, 13–15 September, Portsmouth, UK, pp 333–342, Professional Engineering Publishing Limited, Bury St. Edmunds
- Graham D (1972) An analysis of walking movements in the first instar and adult stick insect. *J Comp Physiol* 81:23–52
- Graham D (1977) Simulation of a model for the coordination of leg movement in free walking insects. *Biol Cybern* 26:187–198
- Graham D (1985) Pattern and control of walking in insects. *Adv Insect Physiol* 18:31–140
- Johnson SD (1994) Simple hybrid systems. *Int J Bifur Chaos* 6:1655–1665
- Müller U, Cruse H (1991) The contralateral coordination of walking legs in the crayfish *Astacus leptodactylus*. *Biol Cybern* 64:437–446
- Pfeiffer F, Eltze J, Weidemann HJ (1995) Six-legged technical walking machine considering biological principles. *Robot Auton Syst* 14:223–232